PCCP

Role of Anderson Rule in Determining Electronic, Optical and Transport Properties of Transition-metal Dichalcogenides Heterostructure

Journal:	*Physical Chemistry Chemical Physics*
Manuscript ID	CP-ART-08-2018-005522.R1
Article Type:	Paper
Date Submitted by the Author:	05-Nov-2018
Complete List of Authors:	Xu, Ke; Fudan University, Department of Optical Science and Engineering Xu, Yuanfeng; Fudan University, Department of Optical Science and Engineering Zhang, Hao; Fudan University, Department of Optical Science and Engineering Peng, Bo; Fudan University Shao, Hezhu; Ningbo Institute of Materials Technology and Engineering, Ni, Gang; Fudan University, Department of Optical Science and Engineering Li, Jing; Fudan University, Dept. of Opt. Sci. & Eng. Yao, Mingyuan; Fudan University, Department of Optical Science and Engineering Lu, Hong-Liang; Fudan University, Department of Microelectronics Zhu, Heyuan; Fudan University, Department of Optical Science and Engineering Soukoulis, Costas; Iowa State University, Division of Materials Science and Engineering

Journal Name

ARTICLE TYPE

Cite this: DOI: 10.1039/xxxxxxxxxx

Role of Anderson Rule in Determining Electronic, Optical and Transport Properties of Transition-metal Dichalcogenides Heterostructures

Ke Xu[1], Yuanfeng Xu[1], Hao Zhang[1†], Bo Peng[1], Hezhu Shao[2‡], Gang Ni[1], Jing Li[1], Mingyuan Yao[1], Hongliang Lu[3], Heyuan Zhu[1¶] and Costas M. Soukoulis[4,5]

Received Date
Accepted Date

DOI: 10.1039/xxxxxxxxxx

www.rsc.org/journalname

Two-dimensional (2D) transition-metal dichalcogenide (TMD) MX_2 (M = Mo, W; X= S, Se, Te) possess unique properties and novel applications in optoelectronics, valleytronics and quantum computation. In this work, we performed first-principles calculations to investigate the electronic, optical and transport properties of the van der Waals (vdW) stacked MX_2 heterostructures formed by two individual MX_2 monolayers. We found that the so-called Anderson's rule can effectively classify the bandstructures of heterostructures to be three types: straddling, staggered and broken gap. The broken gap is gapless, while the other two types possess direct (straddling, staggered) or indirect (staggered) band gaps. The indirect band gaps are formed by the relatively higher energy level of Te-d orbitals, or the interlayer couplings of M or X atoms. For a large part of the formed MX_2 heterostructures, the conduction band maximum (CBM) and valence band minimum (VBM) reside in two separate monolayers, thus the electron-hole pairs are spatially separated, which may lead to bound excitons with extended lifetime. The carrier mobilities, which depend on three competitive factors, i.e. elastic modulus, effective mass and deformation potential constant, show larger values for electron of MX_2 heterostructures compared to their constituent monolayers. Finally, the calculated optical properties reveal strong absorption in the ultraviolet region.

1 INTRODUCTION

The family of two-dimensional (2D) materials has grown rapidly for their unique properties different from their 3D counterparts. A wide range of 2D materials, e.g. graphene[1,2], BN[3,4], transition metal dichalcogenides (TMDs)[5,6], black phosphorus[7–9], and etc, have been proposed and under intense investigations. Among these, transition metal dichalcogenides, with the formula MX_2 (where M is a transition metal and X is a chalcogen), are prominent due to their finite direct band gaps, with strong optoelectronic responses[10], large on-off ratios and high carrier mobilities[11,12]. Furthermore, a spin-orbit driven splitting of the valence band was found in the 2H monolayer TMDs due to the lack of inversion symmetry, which ultimately allows for valley-selective excitation of carriers[13–15]. In addition, the electronic properties of TMDs can be tuned by strain[16], multilayers[17], nanostructuring[18], and electrostatic gating[19], or by combining individual 2D monolayers into van der Waals (vdW) stacked heterostructures[20]. The vdW heterostructures can be obtained by transfer or direct epitaxial growth[21,22]. The interface of the heterostructures is atomically sharp, with two-atomic thick junction region[21], and the interlayer coupling intensity can be further tuned then. Thus, the vdW heterostructures opens up many possibilities for creating new TMD material systems with rich functionalities and novel physical properties[23]. When two different atomically thin layers are stacked and binded by van der Waals forces to form MX_2 heterostructures, electronic properties of the formed vdW MX_2 heterostructures will be significantly affected by the band alignment of the monolayer MX_2, forming various band structures different from the monolayer counterpart, which can be direct- or indirect-bandgap, or metallic materials[24].

Moreover, as we show here, a large part of vdW MX_2 heterostructures possess the band structures with the conduction

[1] Department of Optical Science and Engineering, Key Laboratory of Micro and Nano Photonic Structures (MoE) and Key Laboratory for Information Science of Electromagnetic Waves (MoE), Fudan University, Shanghai 200433, China.
[2] Ningbo Institute of Materials Technology and Engineering, Chinese Academy of Sciences, Ningbo 315201, China
[3] State Key Laboratory of ASIC and System, Institute of Advanced Nanodevices, School of Microelectronics, Fudan University, Shanghai 200433, China
[4] Department of Physics and Astronomy and Ames Laboratory, Iowa State University, Ames, Iowa 50011, USA
[5] Institute of Electronic Structure and Laser (IESL), FORTH, 71110 Heraklion, Crete, Greece
E-mail: †zhangh@fudan.edu.cn
E-mail: ‡hzshao@nimte.ac.cn
E-mail: ¶hyzhu@fudan.edu.cn

band maximum (CBM) and valence band minimum (VBM) residing in different monolayers. Due to the separate spatial locations of CBM and VBM, the photon-generated electron-hole pairs are therefore spatially separated, resulting in much longer exciton lifetime and the possible existence of the interlayer exciton condensation[25], which might help develop two-dimensional lasers, light-emitting diodes and photovoltaic devices[26,27]. The strong interlayer coupling between the two individual monolayer MX_2 in MoS_2-WSe_2 hetero-bilayer was shown to lead to a new photoluminescence (PL) mode[28]. Hong *et al* have also investigated the ultrafast charge transfer in MoS_2-WS_2 heterostructure[29] and found the charge-transfer time is in femtosecond scale, much smaller than that in monolayer MoS_2 or WS_2. Furthermore, the recombination times of interlayer charge transition are tunable for different stacking orders of MoS_2-WS_2 heterostructure, being 39 ps for the one obtained by vertical epitaxial growth and 1.5 ns for the randomly-stacked bilayer, respectively[30].Finally, Tunneling transistors[31] and photovoltaic detector[32] based on MoS_2/$MoTe_2$ heterostructure show excellent performance.

Untill now, most researches on MX_2 heterostructures focus on the S and Se systems.For example, the indirect-to-direct bandgap transition and semiconductor-to-metal transition in MoS_2/MX_2(M = Mo, Cr, W, Fe, V; X = S, Se) heterobilayers can be realized by tensile strain or external electrical field[33]. Hetero-layered TMD (MoS_2,$MoSe_2$,WS_2,WSe_2) with different stacking modes exhibit tunable direct band gaps[24]. Furthermore, Kang *et al* calculated the band offsets of MX_2 heterostructures and found that the MoX_2-WX_2(X = S, Se) heterostructures have type-II band alignment[34]. However, a systemmatic study on vdW MX_2 heterostructures including Te system is still lacking. In this paper, by using first-principles calculations, we theoretically investigate the electronic, mechanical, transport and optical properties of the vdW MX_2 (M = Mo, W; X= S, Se, Te) heterostructures with different stacking modes. The band alignment and interlayer coupling can result in much smaller bandgaps of MX_2 heterostructures compared to those of the constituent MX_2 monolayers, and the direct to indirect bandgap transition may occur. The excellent mechanical properties show the structural stability of the optimized vdW MX_2 heterostructures. The theoretical values of the transport properties are predicted based on the deformation-potential theory. Furthermore, to demonstrate the contribution from monolayer MX_2, the relative relation between MX_2 heterostructures and the constituent monolayers, in respect of elastic modulus, deformation-potential constants and effective masses, is studied in details. Finally, we also point out the strong optical absorption of the vdW MX_2 heterostructures in the ultraviolet region.

2 METHODOLOGY

All the calculations are performed using the Vienna *ab-initio* simulation package (VASP) based on density functional theory (DFT)[35]. The exchange-correlation energy is described by the generalized gradient approximation (GGA) in the Perdew-Burke-Ernzerhof (PBE) parametrization. We choose the DFT-D2/D3 approach to involve the long-distance van der Waals (vdW) interactions[36–39]. The calculation is carried out by using the projector-augmented-wave (PAW) pseudopotential method with a plane-wave basis set with a kinetic energy cutoff of 600 eV. A 15×15×1 Γ-centered **k**-mesh is used during structural relaxation for the unit cell until the energy differences are converged within 10^{-6} eV, with a Hellman-Feynman force convergence threshold of 10^{-4} eV/Å. The vacuum size is larger than 25 Å between two adjacent atomic layers to eliminate artificial interactions between them. The electronic bandstructures of the vdW layered heterostructures are further verified by the calculations using hybrid Heyd-Scuseria-Ernzerhof (HSE06) functional[40,41], which improves the precision of bandstructures by reducing the localization and delocalization errors of PBE and Hartree-Fock (HF) functionals. Here the mixing ratio is 25% for the short-range HF exchange. The screening parameter is 0.2 $Å^{-1}$.

As we know, the electron-phonon scatterings play an important role in determining the intrinsic carrier mobility μ of 2D vdW MX_2 heterostructures, in which the scattering intensities by acoustic phonons are much stronger than those by optic phonons in two-dimensional materials[42]. Therefore, the deformation potential theory for semiconductors, which considers only longitudinal acoustic phonon scattering process in the long-wavelength limit[43–46], and was originally proposed by Bardeen and Shockley[47], can be used to calculate the intrinsic carrier mobility of 2D materials. In the long-wavelength limit, the carrier mobility of 2D semiconductors can be written as[46,48,49]:

$$\mu = \frac{2e\hbar^3 C}{3k_B T |m^*|^2 D_l^2}, \tag{1}$$

where e is the electron charge, $\hbar$ is the reduced Planck's constant, T is the temperature equal to 300 K throughout the paper. C is the elastic modulus of a uniformly deformed crystal by strains and derived from $C = [\partial^2 E/\partial^2(\Delta l/l_0)]/S_0$, in which E is the total energy, Δl represents the change of lattice constant l_0 along the strain direction, and S_0 is the lattice area at equilibrium for a 2D system. m^* is the effective mass given by $m^* = \hbar^2(\partial^2 E(k)/\partial k^2)^{-1}$ (k is wave-vector, and $E(k)$ is the energy).And the spacing of the kmesh we used to calculate the effective masses is 0.02 [$Å^{-1}$]. In addition, D_l is the deformation potential (DP) constant defined by $D_l^{e(h)} = \Delta E_{CBM(VBM)}/(\Delta l/l_0)$, where $\Delta E_{CBM(VBM)}$ is the energy shift of the band edge with respect to the vacuum level under a small dilation Δl of the lattice constant l_0.

3 Results and discussion

3.1 Geometric structures of hetero-bilayer MX_2

Generally, the MX_2 crystals have four stable lattice structures, i.e., 2H, 1T, 1T' and 3R[50], with the first being the dominating one in nature at room temperature. Most MX_2 crystals, like MoS_2 and WSe_2 with a stable 2H phase (1H for monolayer), have been studied widely[51]. For 2H-phase MX_2 crystals, the M atoms and X atoms are located in different layers respectively, which can be described by the point group D_{3h}. While for the 3R-phase unit cell shown as Fig. 1(b,d), one M atom is eclipsed by the X atoms above and the other one is located in the hexagonal center, leading to the AB Bernal stacking. In fact, the electronic structure of the MX_2 heterostructure is sensitive to the stacking modes, due to the different interlayer interactions, and AA and AB stacking structures possess the weakest and strongest interlayer electronic coupling, respectively[52]. For simplicity, we only consider these two stacking modes. However, some interesting properties, e.g. the relatively constant change in both electronic and mechanical couplings at twist angles between 0° (AA stacking) and 60° (AB stacking) found in twisted MoS_2 bilayer[53], and so on, may not be captured by these two modes, which is beyond the scope of our work. One stacking type can be geometrically transformed to the other by horizontal sliding or by the rotation around the vertical axis. For MX_2 heterostructures with two different constituent monolayer MX_2 crystals, both AA and AB stacking crystals possess a lower symmetry of C_{3v} point group, with the symmetry operations of C_3 and vertical mirror reflection σ_v[54] rather than the mirror reflection operation σ_h in the horizontal plane.

To determine the energetically stable structure before geometry optimization, an interlayer-distance optimization algorithm is implemented to reach an optimized d_1 (defined in the Fig. 1(a)) using the Universal Binding Energy Relation (UBER) method, which provides a simple unverisal form for the relation between binding energy and atomic separation[55,56]. The optimized interlayer distance is predicted from a series of unrelaxed models with different d_1 (from 5 to 8 Å), and then we calculate the surface adhesion energy W_{ad} for all 30 types of 2D vdW MX_2 heterostructures under investigations here (e.g. MoS_2/WSe_2 hetero-bilayer),

$$W_{ad} = \frac{E_{MoS_2} + E_{WSe_2} - E_{MoS_2/WSe_2}}{A}, \quad (2)$$

where A is the interface area and E_{MoS_2}, E_{WSe_2}, E_{MoS_2/WSe_2} are the total energies of the monolayer MoS_2, WSe_2 and the MoS_2/WSe_2 heterostructure, respectively. The optimal interlayer distances d_1 can be obtained by maximizing the value of W_{ad}. Then the further structure optimizations are implemented without any external constraints. Furthermore, the formation energy E ($E = E_{AB} - E_A - E_B$) has been listed in TABLE S2. The negative values of the formation energies also confirm the stability of our structures, and for most MX_2 heterostructures AA stacking is more energetically favorable.

The calculated lattice constant a and interlayer distance d for the above-mentioned 30 types of 2D MX_2 heterostructures are summarized in the TABLE 1, which are in good consistence with previous theoretical and experimental results[57–60]. As shown in TABLE 1, the optimized interlayer distances of AA stacking structures are larger than those of the corresponding AB stacking structures, which is due to the fact that, in AB structures, the X atoms are not aligned along the vertical axis and a shorter interlayer distance leads to a smaller total energy. Furthermore, the change of stacking type of heterostructures will affect the interlayer interactions of M or X atoms.

3.2 Electronic band structure of hetero-bilayer MX_2

Previous studies have revealed that the monolayer MX_2 possesses direct band gap, and both the CBM and VBM located at K point in the first Brillouin zone[17,34,63,64]. Owing to the lack of inversion symmetry and the strong spin-orbit coupling (SOC), the valence bands possess a significant spin-orbit splitting at K valleys[65]. And the band alignment for MX_2 shows the following trends (see from Fig. 2(b)): 1) For common-X system, the band gap of MoX_2 are larger than that of WX_2, and the CBM and VBM of WX_2 are higher than those of MoX_2; 2) For common-M system, an increase of the atomic number of X results in a shallower anion p orbital and thus a shift of the VBM to higher energy levels, finally leading to decreased band gaps[66]. To understand these two trends in band alignment, the atomic orbital composition of the states should be taken into consideration. Taking MoS_2 as an example, the CBM of MoS_2 is mainly composed by the d_{z^2} orbital of Mo and the p_x and p_y orbitals of S, whereas the VBM mostly consists of the $d_{x^2-y^2}$ and d_{xy} orbitals of Mo.

For the hetero-bilayer MX_2 crystals constructed by two monolayer MX_2, the formation of their band structures can be understood by the so-called Anderson's rule, which provides the scheme of the construction of energy band diagrams for the heterostructure consisting of two semiconductor materials[67]. According to the Anderson's rule, the vacuum energy levels of the two constituent semiconductors on either side of the heterostructure should be aligned at the same energy[68], and there are three types of possible bandedge lineups: straddling, staggered and broken gap, as shown in Fig. 2(a). For type I heterostructure, the CBM and the VBM mainly consist of the orbitals of semiconductor B, which possesses a smaller band gap compared to semiconductor A. Thus, the band type of the heterostructure is consistent with the smaller-gap material. For type II heterostructure, the VBM and the CBM around the Fermi level reside in two separate semiconductors, and the formed heterostructure still possesses a small direct or indirect band gap. As for type III heterostructure, the locations of CBM and VBM are similar to those of type II heterostructure, but there does not exist band gap, and the formed heterostructure is a semimetal. It should be noted that, for type II and type III heterostructures, since the CBM and VBM may locate in different semiconductors, the photon-generated excitons are thus spatially separated, which will suppress the recombination of electron-hole pairs and extend the exciton lifetime compared with the corresponding individual semicondutors[26,27,34,69–71].

The band structures for the vdW MX_2 heterostructures are calculated by the PBE and HSE06 method and the results, i.e., band types and bandgaps, are shown in TABLE 1. The direct band gap at K point for monolayer MX_2 is transformed into three types of band gaps when a hetero-bilayer MX_2 crystal is formed, i.e., direct, indirect ($M-K, \Gamma-K, K-Q$) and zero bandgap or overlapping bands, according to the calculated results shown in TABLE 1 and the above-mentioned analyses based on the Anderson's rule. The formation types of the band gap for the vdW MX_2 heterostructures categorized according to the Anderson'rule are also shown in TABLE 1. The classification of the band types according to the Anderson's rule is called as Anderson band type hereafter. It is shown in TABLE 1 that, the Anderson band types for the vdW MX_2 are determined by the constituent monolayer MX_2 irrespective of the stacking manner, which is probably due to the fact that the VBM/CBM of hetero-bilayer structure is attributed to the $d/p-$obitals of M/X atoms, and the weak vdW interactions will not change the charge distribution of the constituent monolayers significantly, thus the relative CBM/VBM energies of the con-

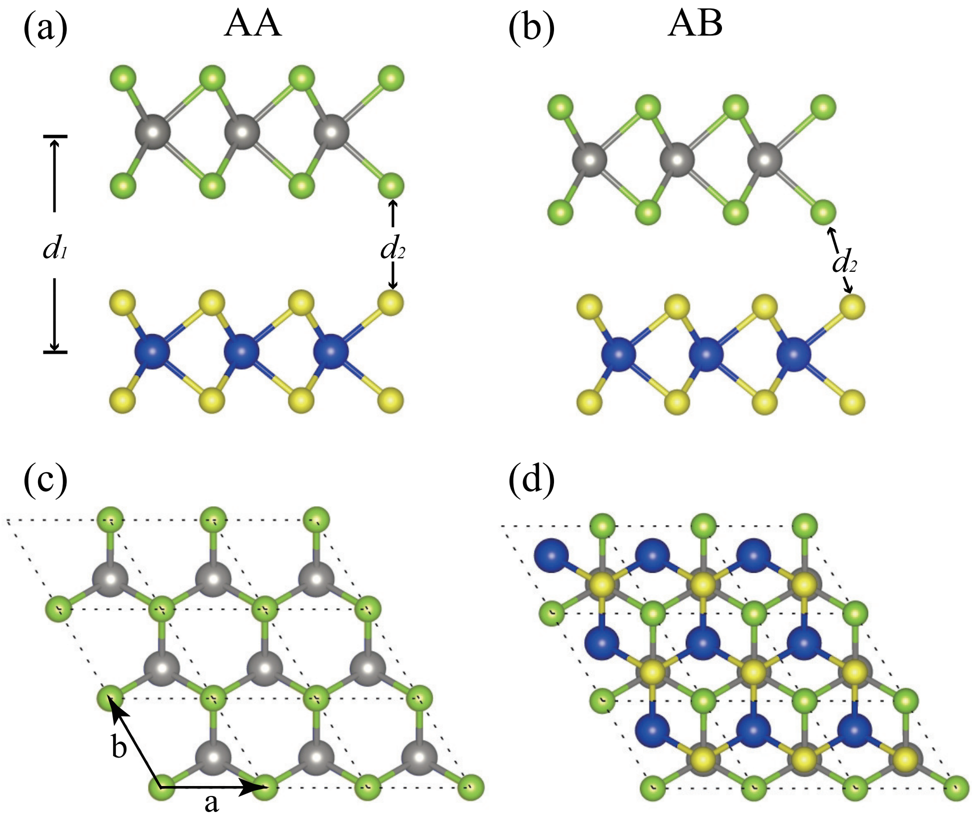

Fig. 1 Atomic structure of AA stacking and AB stacking hetero-bilayer MX_2 in a 3×3×1 supercell from side view (upper panel) and top view (lower panel), respectively. Large and small spheres represent the M and X atoms, respectively. A color coding is used to distinguish the different atomic species. d_1 and d_2 are the interlayer distance (M_1-M_2) and the bond length of X_1-X_2.

stituent monolayers will not change.

For simpilicity, we first consider the Anderson band type I heterostructure, e.g. band structures for WTe_2-WSe_2 and $MoTe_2$-WSe_2 hetero-bilayer shown as Fig. 3(a,b). Generally, as we mentioned above, two monolayer MX_2 crystals with identical M atoms but different X atoms possess different CBM/VBM energy levels, and the crystal with the X atoms with a larger atomic number has a higher energy level of CBM or VBM. However, as shown in Fig. 2(b), the CBM energy level of WTe_2 is lower than that of WSe_2, although the atomic number of Te is larger than Se. Such a deviation can be understood by the fact that the bond length d_{W-Te} of WTe_2 is the largest one among those of the monolayer MX_2 crystals, which leads to a small overlap integral V between d orbitals of M atoms and p orbitals of X atoms for the formation of CBM due to $V \propto 1/d^2_{W-Te}$ [72,73], and thus counteracts the increase of CBM energy level from Se with a swallower p orbitals compared to Te[34]. The smaller CBM energy level of WTe_2 ultimately results in the Anderson band type-I alignment of band edges in WTe_2-WSe_2 hetero-bilayer, leading to a direct bandgap at K point for both AA and AB stacking manners, as shown in Fig. 3(a).

According to TABLE 1, most of the hetero-bilayer MX_2 crystals belong to Anderson band type II heterostructures, e.g., hetero-bilayer MoS_2-WSe_2 and $MoTe_2$-WTe_2. Fig. 3(c) shows the energy band structures of the AA and AB stacking MoS_2-WSe_2 hetero-bilayers, exhibiting direct bandgaps of 0.60eV and 0.75eV for AA and AB stacking type, respectively, which are consistent with the previous results[33]. The CBM locates in the MoS_2 layer and the VBM locates on the WSe_2 layer, resulting in the formation of spatially separated electron-hole pairs. Experiments on hetero-bilayer MoS_2-WSe_2 revealed the dramatically quenching of the photoluminescence (PL) intensities[28], and the extended exciton lifetime[27].

As for the formation of indirect band gaps for type-II heterostructures, there are three types of such indirect band gaps, i.e. $M-K$, $\Gamma-K$ and $K-Q$, resulting from the relatively higher energy level of Te-5p orbital, the relatively stronger $p_z - p_z$ bonds of X atoms in different monolayers, and the hybridization of M-d and X-p orbitals, respectively.

As shown in Fig. 3, the valence band at the M point is attributed to the p_x and p_y orbitals of X atoms, and the corresponding energy level for hetero-bilayer MX_2 crystals containing Te atoms is larger than those only containing Se or S atoms, since the atomic number of Te is the largest one. Therefore, for hetero-bilayer MTe_2-MX_2, the valence band energies at M point significantly increase compared with the hetero-bilayer MSe_2-MX_2 (X≠Te) or MS_2-MX_2 (X≠Te), which subsequently leads to the formation of the $M-K$ indirect band gap, e.g. hetero-bilayer $MoTe_2$-WSe_2, as shown in Fig. 3(b).

The valence band at the Γ point can be attributed to the interlayer overlap integral of p_z orbitals of X atoms belonging to different monolayers at Γ point, as shown in Fig. 3. For hetero-bilayer MX_2 considered here, the distance between X atoms in different

Table 1 Hetero-bilayer system and band alignment type, optimized lattice constant a (Å), interlayer distance d_1 (Å) and the atmoic distance d_2 (Å) between the adjacent anion in different layers, band gap of MX_2 heterostructure (PBE/HSE/SOC).Other theoretical data are also listed in parentheses for comparison

System (Anderson)	Stacking type	a(Å)	d_1 (Å)	d_2(Å)	Band type	$E_g^{PBE}/E_g^{HSE}/E_g^{SOC}$ (eV)
MoS_2-WSe_2 (II)	AA	3.214 (3.22 [61])	6.828	3.573	Direct	0.60(0.57 [62])/1.19/0.37
	AB	3.215	6.164	3.455	Direct	0.75/1.33/0.53
MoS_2-WS_2 (II)	AA	3.183 (3.18 [57])	6.758 (6.8 [58])	4.826	Indirect	1.29(1.16 [62])/1.93/1.22
	AB	3.187	6.137 (6.3 [58])	3.535	Indirect	1.08/1.70/1.06
WS_2-WSe_2 (II)	AA	3.213 (3.204 [24])	6.864	4.808	Direct	0.93(1.007 [24])/1.43/0.67
	AB	3.212	6.229	3.503	Direct	1.05/1.56/0.80
$MoSe_2$-WS_2 (II)	AA	3.211 (3.210 [24])	6.877	4.820	Direct	1.13 (1.154 [24])/1.53/1.00
	AB	3.212	6.295	3.570	Direct	1.09 /1.48/0.97
$MoSe_2$-WSe_2 (II)	AA	3.279 (3.277 [24])	7.019 (6.62 [59])	4.913	Indirect	1.30 (1.330 [24])/1.86/1.03
	AB	3.279	6.362(6.48 [59])	3.554	Indirect	1.28/1.77/1.09
MoS_2-$MoSe_2$ (II)	AA	3.250 (3.26 [62])	6.972	4.940	Direct	0.98(0.74 [62])/1.10/0.56
	AB	3.254	6.350	3.655	Direct	0.65/1.09/0.56
$MoTe_2$-MoS_2 (II)	AA	3.328	7.267	5.058	–	–/0.45/–
	AB	3.347	6.575	3.736	–	–/0.47/–
$MoTe_2$-$MoSe_2$ (II)	AA	3.413	7.421	5.177	Indirect	0.49/0.95/0.19
	AB	3.413	6.784	3.853	Indirect	0.51/0.95/0.21
$MoTe_2$-WS_2 (II)	AA	3.347	7.170	4.984	–	–/0.43/–
	AB	3.350	6.576	3.757	–	–/0.42/–
$MoTe_2$-WSe_2 (I)	AA	3.425	7.354	5.136	Indirect	0.69/1.05/0.60
	AB	3.423	6.725	3.811	Indirect	0.64/1.00/0.53
$MoTe_2$-WTe_2 (II)	AA	3.538(3.56 [60])	7.646	5.348	Direct	0.95/1.44/0.67
	AB	3.543	6.954	3.923	Indirect	0.93/1.46/0.74
WTe_2-MoS_2 (III)	AA	3.354	7.204	5.018	–	–/0.46/–
	AB	3.358	6.584	3.751	–	–/0.37/–
WTe_2-$MoSe_2$ (II)	AA	3.423	7.358	5.128	Direct	0.33/0.85/0.10
	AB	3.429	6.740	3.833	Direct	0.35/0.84/0.11
WTe_2-WS_2 (III)	AA	3.360	7.114	4.963	–	–/0.41/–
	AB	3.365	6.516	3.717	–	–/0.40/–
WTe_2-WSe_2 (I)	AA	3.422	7.288	5.092	Direct	0.51/0.93/0.24
	AB	3.447	6.679	3.781	Direct	0.45/0.86/0.17

monolayers for the AB stacking hetero-bilayer, i.e. d_2 shown in Fig. 1(a,b), is smaller than the corresponding AA stacking hetero-bilayer, as shown in TABLE 1, thus the energy level of the valence band at the Γ point for the former is the higher one, due to $V_{p_z-p_z} \propto 1/d_2^2$. The increase of the energy level of the valence band at Γ points sometimes leads to the formation of $\Gamma-K$ indirect band gap with AB stacking, e.g. AB-stacking $MoTe_2$-WTe_2 as shown in Fig. 3(d).

Another indirect band gap ($K-Q$), .e.g $MoSe_2$-WSe_2 shown as Fig. S2, is formed by VBM located at K point and CBM located at Q point between Γ and K. According to the analysis on the atomic orbitals, the energy level of the valence band at Q point is formed by the strong hybridization between the Mo-d orbitals and W-d orbitals, which lowers the energy level at Q point and ultimately leads to the shift of CBM from K to Q point[74]. However, the CBM and VBM at K are insignificantly hybridized, due to the higher symmetry and a larger bond length d_{Mo-W} compared to those at Q point[57], thus the VBM is fixed at K point.

The extreme state of staggering is the formation of broken bandgaps, which is also called as the Anderson band type III alignment, as shown in Fig. 2(a). For example, the CBMs of MoS_2 and WS_2 are much lower than that of other monolayer MX_2 and the WTe_2 possess the highest VBM, as shown in Fig. 2(b), the band alignment in hetero-bilayer WTe_2-MoS_2 and WTe_2-WS_2 thus can be approximately considered as the Anderson band type III alignment, as shown in Fig. 3(e,f). The band overlaps at K point, changing the heterostructures into metallic phase.

The bandgaps of the hetero-bilayer MX_2 crystals based on the HSE06 and SOC calculations are also provided in TABLE 1. The negative SOC effects decrease the band gap and the HSE calculations increase the band gap by 0.4-0.6 eV, compared to PBE calculations. It should be noted that the metallic phases of the hetero-bilayer MX_2 crystals, i.e. the Anderson band type III heterostructures, e.g. hetero-bilayer WTe_2-MoS_2 and WTe_2-WS_2 crystals as shown in Fig. 3(e,f), are replaced by direct band gap based on HSE calculations, which means that the hetero-bilayer MX_2 crystals considered here does not possess the Anderson band type III alignment.

In summary, the CBM state at K point is weakly localized and not affected by the stacking types usually. While the VBM may shift from K to Γ point in regard to different stacking types due to the interlayer electronic coupling. And Kang *et al* have stated that the interlayer coupling strength of AB configuration at Γ point is the strongest among the heterostructures with arbitrary in-plane angular rotations to push the band energy at Γ point up to a highest level[75]. In contrast, the interlayer coupling strength of AA configuration (0 degree) is the weakest. And this argument can be proved by the Moiré pattern of these heterostructures to demonstrate that the pattern becomes smaller and more complex with the rotation angle θ increasing. Moreover, this Moiré pattern-induced wave function localization of VBM will significantly affect the carrier mobilities of MX_2 heterostructures, as it will be discussed in the next section.

3.3 Mechanical properties and transport properties of hetero-bilayer MX_2

Since the MX_2 heterostructures under considerations here possess C_{3v} symmetry, the number of independent second-order elastic coefficients c_{ij} is five and $c_{11} = c_{22}$[76]. The calculated elastic coefficients of all MX_2 heterostructures are shown in TABLE S2, and all the vdW MX_2 heterostructures are mechanically stable, according to the Born criteria[77],

$$C_{11} - C_{12} > 0, C_{11} + 2C_{12} > 0, C_{44} > 0 \tag{3}$$

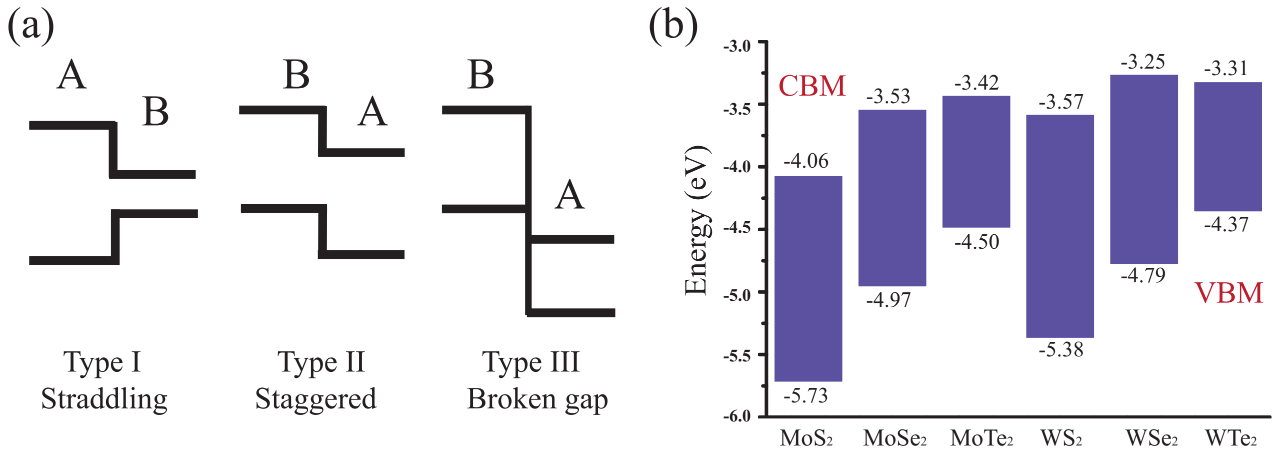

Fig. 2 (a) Various possible bandedge lineups in semiconductor A and B. (b) Band alignment for monolayer MX_2.The vacuum level is taken as 0 reference.

Table 2 Hetero-bilayer system and band alignment type, Young's modulus $Y(GPa)$ and Poisson's ratio v , electron and hole effective masses along armchair direction, deformation potential constants for CBM and VBM, elastic modulus, electron and hole mobilities along armchair direction.

System (Anderson)	Stacking type	$Y(N/m)$	v	$m_e^*(m_0)$	$m_h^*(m_0)$	D_l^e	D_l^h	C (N/m)	μ_e(cm^2/(V·s))	μ_h (cm^2/(V·s))
MoS_2-WSe_2 (II)	AA	217.58	0.25	0.47	0.47	3.05	3.26	139.55	961.16	875.94
	AB	211.03	0.27	0.48	0.46	4.05	2.43	152.92	573.03	1808.89
MoS_2-WS_2 (II)	AA	241.46	0.25	0.46	1.70	6.01	5.70	127.81	256.46	18.04
	AB	242.03	0.24	0.46	0.92	6.28	5.03	121.19	318.08	76.70
WS_2-WSe_2 (II)	AA	229.08	0.26	0.30	0.47	3.44	3.60	149.27	1990.11	770.94
	AB	226.75	0.26	0.26	0.45	4.85	2.38	151.14	1345.29	1947.10
$MoSe_2$-WS_2 (II)	AA	261.16	0.31	0.28	0.62	3.26	3.38	152.12	2575.74	511.18
	AB	272.66	0.32	0.29	0.58	5.09	1.87	92.47	600.18	1158.73
$MoSe_2$-WSe_2 (II)	AA	218.88	0.27	0.67	0.45	4.29	1.59	130.84	224.10	3752.36
	AB	212.42	0.28	0.61	1.12	1.93	2.84	122.16	1239.06	177.56
MoS_2-$MoSe_2$ (II)	AA	232.78	0.26	0.42	0.71	2.87	2.78	125.83	1321.55	454.69
	AB	230.26	0.27	0.42	0.71	3.07	4.50	114.86	758.03	359.04
$MoTe_2$-MoS_2 (II)	AA	196.82	0.36							
	AB	196.87	0.34							
$MoTe_2$-$MoSe_2$ (II)	AA	184.77	0.31	0.46	1.37	4.40	3.74	113.18	532.75	45.79
	AB	200.46	0.25	0.46	1.37	4.07	3.75	110.81	532.75	45.79
$MoTe_2$-WS_2 (II)	AA	206.17	0.28							
	AB	195.86	0.31							
$MoTe_2$-WSe_2 (I)	AA	183.70	0.28	0.30	1.33	3.95	3.83	109.1	515.87	52.52
	AB	194.71	0.24	0.30	1.25	4.41	4.14	114.79	1191.02	58.76
$MoTe_2$-WTe_2 (II)	AA	136.33	0.39	0.57	0.42	1.61	1.38	101.62	1023.61	55.76
	AB	171.83	0.22	0.58	3.46	4.32	3.30	99.43	2315.94	3285.72
WTe_2-MoS_2 (III)	AA	169.33	0.20							
	AB	189.09	0.28							
WTe_2-$MoSe_2$ (II)	AA	183.83	0.27	0.45	0.48	2.65	2.85	109.47	382.87	6.58
	AB	196.41	0.22	0.45	0.48	2.70	2.85	102.26	912.5	987.31
WTe_2-WS_2 (III)	AA	189.00	0.20							
	AB	233.27	0.29							
WTe_2-WSe_2 (I)	AA	168.36	0.33	0.30	0.46	2.95	2.97	113.4	912.5	987.31
	AB	197.77	0.22	0.30	0.45	2.79	3.08	115.65	875.3	918.66

The 2D Young's modulus of all MX_2 heterostructures, given by $Y^{2D} = \frac{c_{11}c_{22}-c_{12}^2}{c_{11}}$ [78], are listed in TABLE 2. The 2D Young's modulus for monolayer MX_2 crystals decrease from MS_2 to MSe_2 to MTe_2 [79], which is due to the fact that, the strength of $d_{xy,yz,zx}-p$-orbital coupling, which forms M-X bonding, becomes weaker with an increase of the atomic number of chalcogen[80]. The calculated 2D Young's modulus for monolayer MX_2 crystals are shown in TABLE S1. The contributions to the mechanical properties of MX_2 heterostructures can be roughly considered from constituent monolayer MX_2 crystals and the weak interlayer bonding.

The Young's modulus of the MTe_2-MX_2 heterostructures are lower than others due to the weakest Y^{2D} of monolayer MTe_2 among the monolayer MX_2 crystals considered here. Meanwhile, the Young's modulus of the MX_2 heterostructures are a little lower than the sum of those of the constituent monolayer MX_2 crystals, which means that the contribution from the interlayer bonding to the total Young's modulus is negative. The Poisson's ratios given by $v^{2D} = \frac{c_{12}}{c_{22}}$ [78], which describes the lateral deformation when applying uniaxial strains, are calculated and shown in TABLE 2. Generally materials with high Poisson's ratio possess good plasticity. The Poisson's ratios for the MX_2 heterostructures are numerically close to each other except WTe_2-MX_2, due to the lowest Poisson's ratio of 0.20 of monolayer WTe_2 crystal among the monolayer MX_2 crystals (see TABLE S1).

The effective masses for electrons m_e^* and holes m_h^* of vdW MX_2 heterostructures along armchair and zigzag directions are calculated respectively, and the results along armchair direction are shown in TABLE 2. The values of m_e^* for AA-stacking MX_2 heterostructures are close to those of the corresponding AB-stacking ones, however, the values of m_h^* for AA-stacking heterostructures are deviated obviously from those of AB-stacking ones, e.g. MoS_2-WS_2 and $MoTe_2$-WTe_2 heterostructures, especially when the band

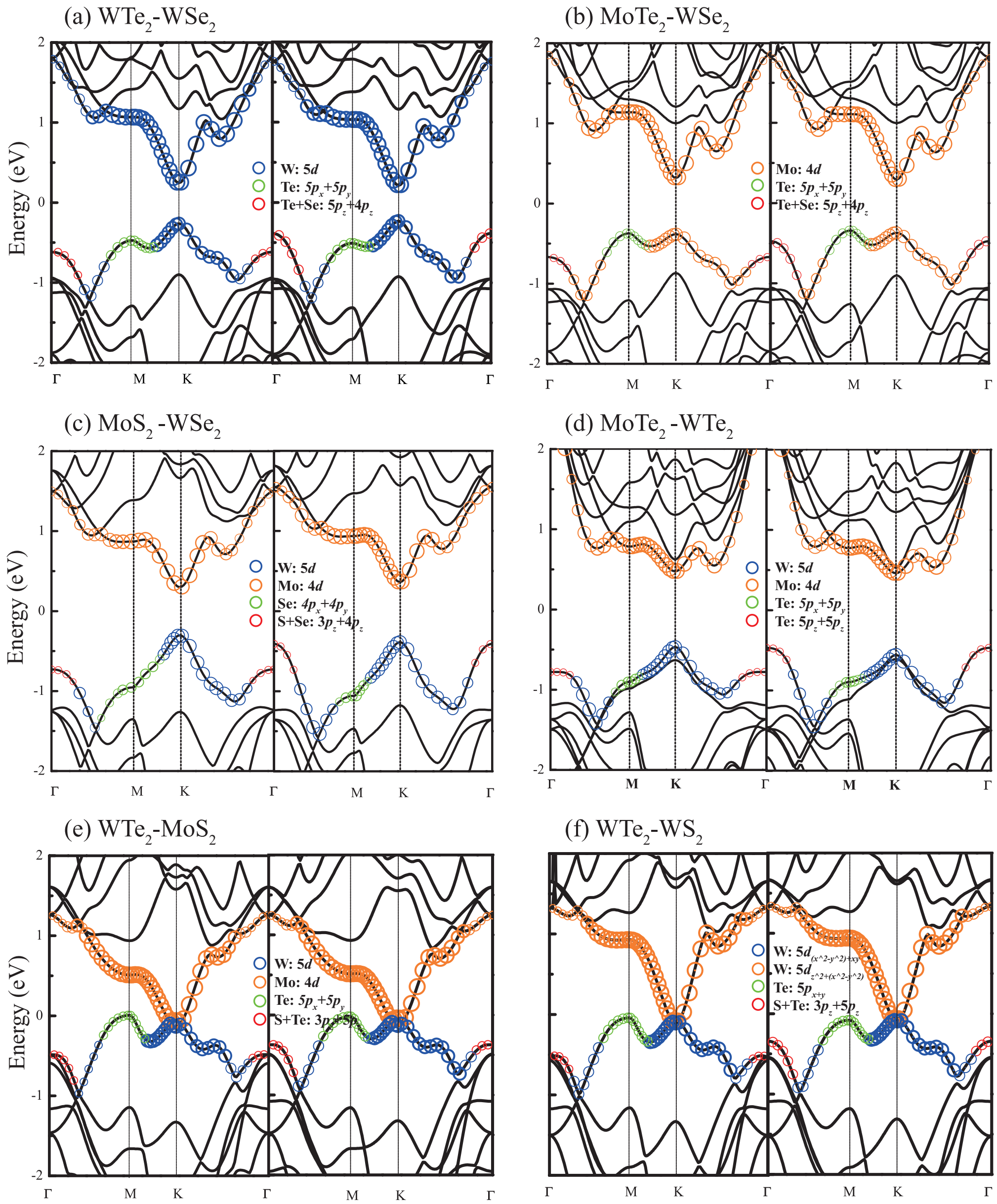

Fig. 3 Band structures of the AA and AB stacking vdW MX_2 heterostructures and atomic orbital weights in the energy bands. The blue and orange circles represent d orbitals of the cations. The green and red circles represent $p_x + p_y$ and p_z orbitals of the anions, respectively. The size of each circle is proportional to the weight of the atomic orbital. (a)(b) Type I band alignment system: WTe_2-WSe_2 and $MoTe_2$-WSe_2 hetero-bilayer. (c)(d)Type II band alignment system: MoS_2-WSe_2 and $MoSe_2$-WSe_2 hetero-bilayer. (e)(f)Type III band alignment system: WTe_2-MoS_2 and WTe_2-WS_2 hetero-bilayer.

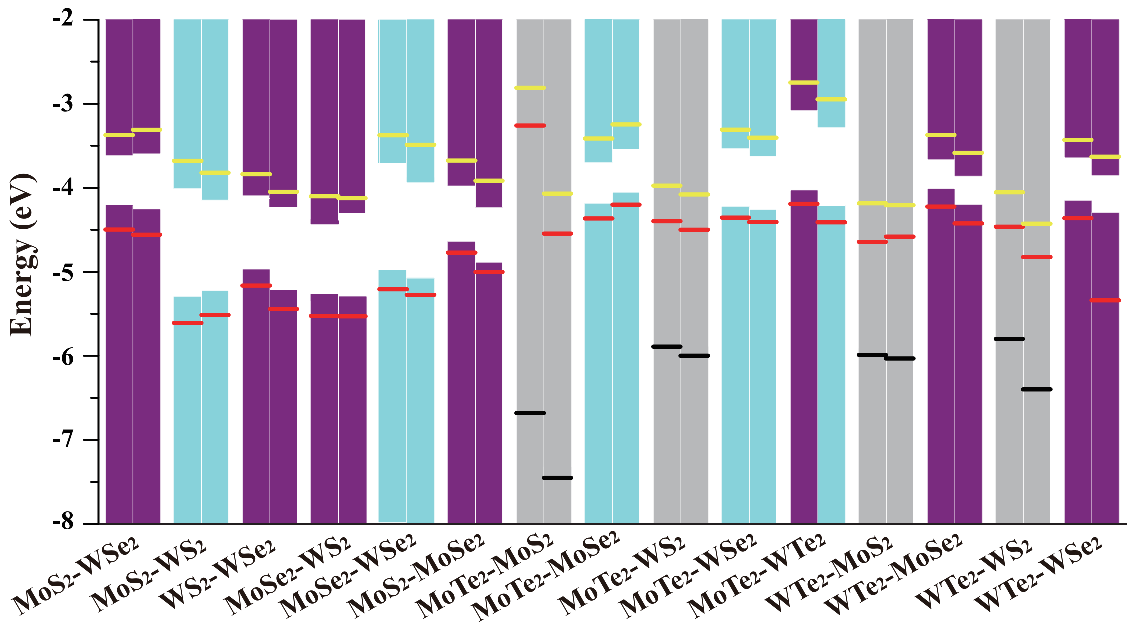

Fig. 4 Calculated band alignment for the vdW MX_2 heterostructures. The histogram is obtained by PBE, with the purple, blue and grey representing the direct bandgap, indirect bandgap and zero-bandgap, respectively. The red and yellow solid lines represent the VBM and the CBM obtained by HSE.

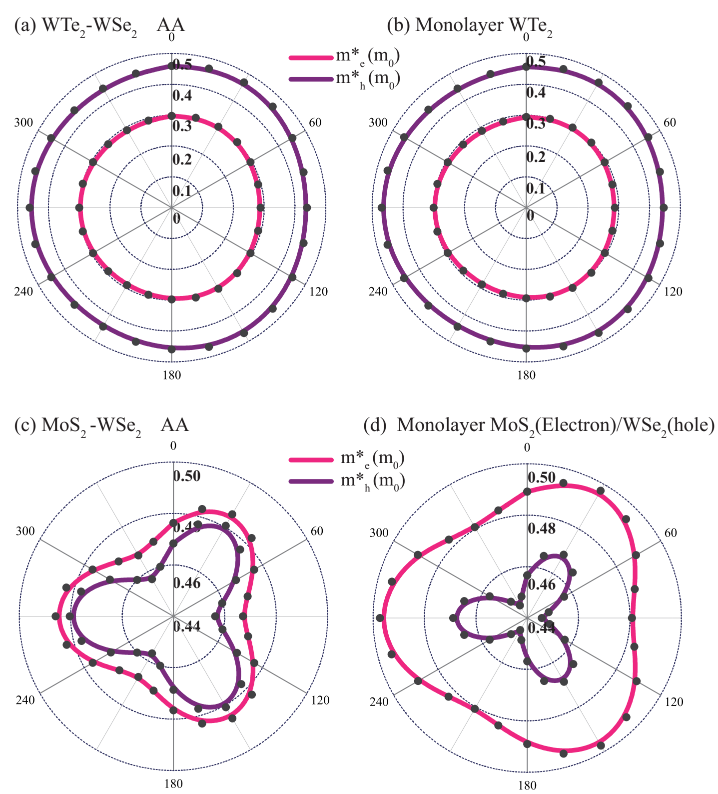

Fig. 5 The calculated carrier (hole mass$_h^*$ and electron mass$_e^*$) for (a) Type I band alignment system (WTe_2-WSe_2 hetero-bilayer), (b) monolayer WTe_2, (c)Type II band alignment system (MoS_2-WSe_2 hetero-bilayer), (d) monolayer MoS_2 (electron) and WSe_2 (hole)

types for AA and AB stackings are different (direct vs indirect), as shown in TABLE 1 and 2. Such phenomena can be understood by the fixed CBM (electrons) at K or Q point for all the MX_2 heterostructures, and the transition of VBM (holes) from K point to M or Γ point for MX_2 heterostructures with an indirect band gap.

As mentioned above, the bandstructures of MX_2 heterostructures can be roughly decomposed into those of the constituent monolayer MX_2 crystals, according to the Anderson's rule, which also leads to the formation of the effective masses of electrons and holes for MX_2 heterostructures. Fig. 5 shows the effective masses of electrons and holes for MX_2 heterostructures and the corresponding constituent monolayer MX_2 crystals along all directions, taking WTe_2-WSe_2 and MoS_2-WSe_2 hetero-bilayer as examples without loss of generality.

The WTe_2-WSe_2 hetero-bilayer belongs to the Anderson band type I and the CBM and VBM are attributed to those of monolayer WTe_2 crystal. It is shown in Fig. 5(a,b) that the effective masses of electrons and holes for the WTe_2-WSe_2 hetero-bilayer are close to those of monolayer WTe_2 crystals, respectively. However, for MoS_2-WSe_2 hetero-bilayer (Anderson band type II), since the CBM is attributed to that of monolayer MoS_2 crystal and VBM is attributed to that of monolayer WSe_2 crystal, therefore, the m_e^* for MoS_2-WSe_2 hetero-bilayer is similar to that of monolayer MoS_2 and the m_h^* is similar to that of monolayer WSe_2, as shown in Fig. 5(c,d).

According to Eq. (1), the third factor determining carrier mobilites μ is the deformation potential constants, $D_l^{e,h}$, which describes the scatterings of electrons/holes by longitudinal acoustic phonons. The calculated $D_l^{e,h}$ for MX_2 heterostructures and monolayer MX_2 crystals are shown in TABLE 2 and TABLE S1, respectively. By comparison, it is found that, the deformation potential constants of MX_2 heterostructures are overally larger than those of constituent monolayer MX_2, which means that, the formation of the vdW MX_2 heterostructures increases the electron-acoustic phonon coupling, leading to the increase of deformation potential constant D_l, especially for MoS_2-WS_2 heterostructures.

Since the CBM and VBM of the MX_2 heterostructures can be attributed to the respective band structures of the constituent monolayer MX_2, according to the Anderson rule, the shift of VBM from K point to Γ/M point will result in dramatic change of the deformation potential constants and hole effective masses for MX_2 heterostructures with indirect bandgaps, e.g. $MoTe_2$-WTe_2.

In order to figure out the exact contributions from the three factors, i.e. effective masses $m_{e,h}^*$, deformation potential constants $D_l^{e,h}$ and elastic modulus C, to the carrier mobilities μ, compared to the constituent monolayer MX_2 crystals, we plot the values of the three factors for constituent monolayer crystals and hetero-bilayer structures in Fig. S4. It is clear that the elastic modulus of hetro-bilayer structures is nearly twice of the constituent monolayer MX_2 crystals, while the deformation potential constants of hetro-bilayer structures are overally larger or close to the constituent monolayer MX_2 crystals. Moreover, the effective masses of hetro-bilayer structures mostly determined by the constituent monolayer cystals, are thus close to those of constituent monolayer cystals, except some hetro-bilayer structures with VBM points shifted from K to Γ/M, e.g. $MoTe_2$-WTe_2. Finally, the carrier mobility of electrons and holes along armchair and zigzag directions for the MX_2 hetero-bilayer can be calculated according to Eq.(1), as shown in Fig. 6. Fig. 6(a-b) and (c-d) show electron/hole mobilities along armchair and zigzag directions respectively. The mobilities for monolayer MX_2 as a contrast are shown as color blocks in the diagonal direction, and the color blocks in the lower/upper triangular part correspond to the cases of AA/AB-stacking types. For example, the red block of the 1^{st} row and 4^{th} column in Fig.6(a) corresponds to the electron mobilities along armchair direction of AB-stacking MoS_2-WSe_2 heterostructure, i.e. $\mu = 573$ $cm^2/(V{\cdot}s)$. The electron mobilities of hetro-bilayer structures are overally larger than those of constituent monolayer MX_2 crystals, and the same situation takes place for the holes mobilities of hetro-bilayer structures with VBM located at K point. However, the holes mobilities of hetro-bilayer structures with VBM located at Γ/M point are smaller than those of constituent monolayer MX_2 crystals.

The AA stacked $MoTe_2$-$MoSe_2$ heterostructure possesses the highest electron mobility along zigzag direction, i.e. 3658 $cm^2/(V{\cdot}s)$, and the AA stacked $MoSe_2$-WSe_2 heterostructure possesses the highest hole mobility along the armchair direction, i.e. 3752 $cm^2/(V{\cdot}s)$.

3.4 Optical properties of hetero-bilayer MX_2

The optical properties of the vdW MX_2 heterostructures are described by the complex dielectric function, *i.e.* $\varepsilon(\omega) = \varepsilon_1(\omega) + i\varepsilon_2(\omega)$. The imaginary part of dielectric tensor $\varepsilon_2(\omega)$ is determined by a summation over empty band states as follows[81,82],

$$\varepsilon_2(\omega) = \frac{2\pi e^2}{\Omega\varepsilon_0}\sum_{k,v,c}\delta(E_k^c - E_k^v - \hbar\omega)\left|\langle\Psi_k^c|\mathbf{u}\cdot\mathbf{r}|\Psi_k^v\rangle\right|^2, \quad (4)$$

where Ω is the crystal volume, ε_0 is the vacuum dielectric constant, $\hbar\omega$ represents the photon energy, v and c mean the valence and conduction bands respectively, $\mathbf{u}$ is the polarization vector in the incident electric field, $\mathbf{u}{\cdot}\mathbf{r}$ is the momentum operator, Ψ_k is the wave function at the k point. The real part of dielectric tensor $\varepsilon_1(\omega)$ is obtained by the well-known Kramers-Kronig relation[83],

$$\varepsilon_1(\omega) = 1 + \frac{2}{\pi}P\int_0^\infty \frac{\varepsilon_2(\omega')\omega'}{\omega'^2 - \omega^2 + i\eta}d\omega', \quad (5)$$

where P denotes the principle value. Based on the complex dielectric function, the absorption coefficient $\alpha(\omega)$ is given by[84,85]

$$\alpha(\omega) = \frac{\sqrt{2}\omega}{c}\left\{\left[\varepsilon_1^2(\omega) + \varepsilon_2^2(\omega)\right]^{1/2} - \varepsilon_1(\omega)\right\}^{\frac{1}{2}}, \quad (6)$$

In 2D semiconductor materials, the band gap obtained by HSE06 is usually close to the real optical band gap due to the underestimation of band gap by neglecting excitonic effects[86]. Thus, we only performed HSE06 calculations to obtain optical properties for the hetero-bilayer MX_2 under considerations here, which show that all of them are semiconductors with a finite band gap, as shown in TABLE 1. All the optical constants are calculated for incident radiations with the electric field vector **E** polarized

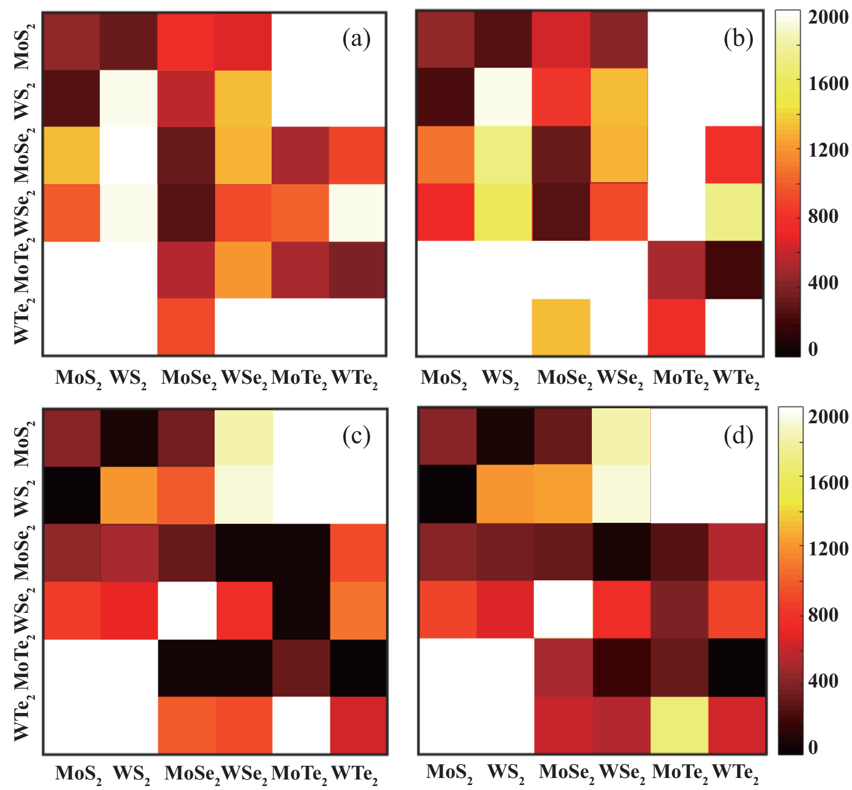

Fig. 6 The calculated carrier mobilities for the vdW MX_2 heterostructures, with the AA stacking's in lower left corner and AB stacking's upper right corner respectively. The values along diagonal are the mobilities for monolayer MX_2.(a)(b) are the electron mobilities of the vdW MX_2 heterostructures along armchair and zigzag directions, respectively; (c)(d) are the hole mobilities of the vdW MX_2 heterostructures along armchair and zigzag directions, respectively.

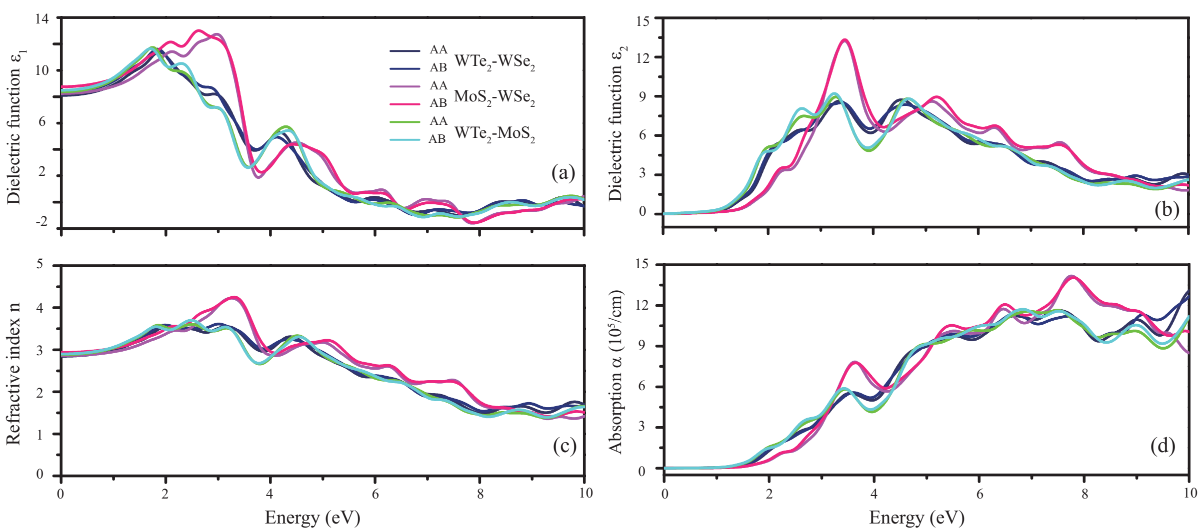

Fig. 7 HSE06 calculations of (a) the real part of the dielectric function, (b) the imaginary part of the dielectric function, (c) refractive and (d) optical absorption spectra of AA and AB stacking hetero-bilayer WTe_2-WSe_2, MoS_2-WSe_2 and WTe_2-MoS_2 for incident light with the polarization along the a.

along the a and b directions[87] shown in Fig. 1(c).

Due to the C_3 symmetry of hexagonal structure of the hetero-bilayer MX_2, the dielectric function $\varepsilon(\omega)$ possesses the same results along the a and b directions. And the $\varepsilon(\omega)$ results for AA and AB stacking type are also close to each other, as shown in Fig. 7(a,b) and Fig. S4, irrrespective of the corresponding Anderson band type. The similarity in $\varepsilon(\omega)$ results between AA and AB stacking hetero-bilayer MX_2 can be understood by the fact that, the bandstructure of the hetero-bilayer MX_2 can be roughly decomposed into the respective bandstructures of the constituent monolayer MX_2 according to the Anderson'rule, thus the contribution to the total optical response, i.e. $\varepsilon_2(\omega)$, from absorption of an incident photon $\hbar\omega$ and then transition from Ψ_k^c to Ψ_k^v can be traced back to the behaviors of electrons located within the constituent monolayer MX_2. Therefore, the $\varepsilon_2(\omega)$ results for AA and AB stacking hetero-bilayer MX_2 probably are similar since they contain identical constituent monolayer MX_2, according to Eq. (4).

The optical properties of hetero-bilayer MX_2, e.g. WTe_2-WSe_2, MoS_2-WSe_2 and WTe_2-MoS_2, are shown in Fig. 7. The main absorption peaks of these three hetero-bilayer MX_2 locate in the range of 3.0 to 5.0 eV, i.e. the ultraviolet region, with a refractive range from 2.80 to 4.27 in this region.

4 Conclusion

In this work, we have investigated the structure, electronic, mechanical, transport and optical properties of the vdW MX_2 heterostructures using first-principles calculations. The AA and AB stacked hetero-bilayer MX_2 exhibit three types of band alignment according to Anderson's rule, with a wide band gap range between 0 and 2 eV. The main differences between AA and AB stacked hetero-bilayer MX_2 lie in the band structure and mechanical properties due to the interlayer coupling such as the indirect $\Gamma - K$ bandgap. The band structure of the MTe_2-MX_2 will possesses a higher valance band at M point due to the high band energy of $5p_{x,y}$ orbitals of Te. The type II band alignment of the vdW hetero-bilayer MX_2 make interlayer transitions possible, leading to spatially separated excitons. The transport properties of the vdW MX_2 heterostructures are consistent with the symmetry of the geometric structures. It should be noted that the carrier mobilities of the hetero-bilayer MX_2 are often higher than those of monolayer MX_2, attributed to the higher elastic modulus for the hetero-bilayer MX_2, while the hetero-bilayer MX_2 with indirect bandgap possess much lower hole mobilities due to the increased effective masses and deformation potential constants. Furthermore, the calculated optical properties show strong optical absorption for vdW MX_2 heterostructures, enabling the novel applications in optoelectronics from visible to ultraviolet region, such as photodetectors, light-emitting diodes, and photovoltaics.

Acknowledgement

This work is supported by the National Natural Science Foundation of China under Grants No. 11374063 and 11404348, the National Basic Research Program of China (973 Program) under Grant No. 2013CBA01505, and FDUROP (Fudan's Undergraduate Research Opportunities Program) under No.16066. Work at Ames Laboratory is partially supported by the U.S.Department of Energy, Office of Basic Energy Science, Division of Materials Science and Engineering (Ames Laboratory is operated for the U.S. Department of Energy by Iowa State University under Contract No. DE-AC02-07CH11358). The European Research Council under ERC Advanced Grant No. 320081 (PHOTOMETA) supports work at FORTH.

References

1 K. S. Novoselov, A. K. Geim, S. V. Morozov, D. Jiang, Katsnelson M. I., I. V. Grigorieva, and A. A. Dubonos, S. V.and Firsov. Two-dimensional gas of massless dirac fermions in graphene. *Nature*, 438:197–200, 2005.

2 Horst L. Stormer Yuanbo Zhang, Yan-Wen Tan and Philip Kim. Experimental observation of the quantum hall effect and berry's phase in graphene. *Nature*, 438, 2005.

3 C. R. Dean, A. F. Young, I. Meric, C. Lee, L. Wang, S. Sorgenfrei, K. Watanabe, T. Taniguchi, P. Kim, K. L. Shepard, and J. Hone. Boron nitride substrates for high-quality graphene electronics. *Nature Nanotechnology*, 5(10):722–726, aug 2010.

4 Matthew Yankowitz, Jiamin Xue, Daniel Cormode, Javier D. Sanchez-Yamagishi, K. Watanabe, T. Taniguchi, Pablo Jarillo-Herrero, Philippe Jacquod, and Brian J. LeRoy. Emergence of superlattice dirac points in graphene on hexagonal boron nitride. *Nature Physics*, 8(5):382–386, mar 2012.

5 B. Radisavljevic, A. Radenovic, J. Brivio, V. Giacometti, and A. Kis. Single-layer mos2 transistors. *Nat. Nanotechnol.*, 6:147–150, 2011.

6 Andrea Splendiani, Liang Sun, Yuanbo Zhang, Tianshu Li, Jonghwan Kim, Chi-Yung Chim, Giulia Galli, and Feng Wang. Emerging photoluminescence in monolayer mos_2. *Nano Lett.*, 10(4):1271–1275, 2010.

7 Du Xiang, Cheng Han, Jing Wu, Shu Zhong, Yiyang Liu, Jiadan Lin, Xue-Ao Zhang, Wen Ping Hu, Barbaros èĎřzyilmaz, A. H. Castro Neto, Andrew Thye Shen Wee, and Wei Chen. Surface transfer doping induced effective modulation on ambipolar characteristics of few-layer black phosphorus. *Nature Communications*, 6(1), mar 2015.

8 Likai Li, Yijun Yu, Guo Jun Ye, Qingqin Ge, Xuedong Ou, Hua Wu, Donglai Feng, Xian Hui Chen, and Yuanbo Zhang. Black phosphorus field-effect transistors. *Nat. Nanotechnol.*, 9(5):372–377, 2014.

9 Vy Tran, Ryan Soklaski, Yufeng Liang, and Li Yang. Layer-controlled band gap and anisotropic excitons in few-layer black phosphorus. *Physical Review B*, 89(23), jun 2014.

10 Marco Bernardi, Maurizia Palummo, and Jeffrey C. Grossman. Extraordinary sunlight absorption and one nanometer thick photovoltaics using two-dimensional monolayer materials. *Nano Letters*, 13(8):3664–3670, jul 2013.

11 D. Hennig and C. Mulhern. Collective transport of coupled particles. *The European Physical Journal B*, 85(1), jan 2012.

12 Wenxu Zhang, Zhishuo Huang, Wanli Zhang, and Yanrong Li. Two-dimensional semiconductors with possible high room temperature mobility. *Nano Research*, 7(12):1731–1737, sep

2014.

13 Ting Cao, Gang Wang, Wenpeng Han, Huiqi Ye, Chuanrui Zhu, Junren Shi, Qian Niu, Pingheng Tan, Enge Wang, Baoli Liu, and Ji Feng. Valley-selective circular dichroism of monolayer molybdenum disulphide. *Nature Communications*, 3(1), jan 2012.

14 Hualing Zeng, Junfeng Dai, Wang Yao, Di Xiao, and Xiaodong Cui. Valley polarization in mos2 monolayers by optical pumping. *Nat Nano*, 7(8):490–493, August 2012.

15 Filip A. Rasmussen and Kristian S. Thygesen. Computational 2d materials database: Electronic structure of transition-metal dichalcogenides and oxides. *The Journal of Physical Chemistry C*, 119(23):13169–13183, jun 2015.

16 Hiram J. Conley, Bin Wang, Jed I. Ziegler, Richard F. Haglund, Sokrates T. Pantelides, and Kirill I. Bolotin. Bandgap engineering of strained monolayer and bilayer MoS2. *Nano Letters*, 13(8):3626–3630, jul 2013.

17 Kin Fai Mak, Changgu Lee, James Hone, Jie Shan, and Tony F. Heinz. Atomically thin mos_2: A new direct-gap semiconductor. *Phys. Rev. Lett.*, 105:136805, Sep 2010.

18 Thomas G. Pedersen, Christian Flindt, Jesper Pedersen, Niels Asger Mortensen, Antti-Pekka Jauho, and Kjeld Pedersen. Graphene antidot lattices: Designed defects and spin qubits. *Physical Review Letters*, 100(13), apr 2008.

19 Qihang Liu, Linze Li, Yafei Li, Zhengxiang Gao, Zhongfang Chen, and Jing Lu. Tuning electronic structure of bilayer MoS2 by vertical electric field: A first-principles investigation. *The Journal of Physical Chemistry C*, 116(40):21556–21562, sep 2012.

20 K. S. Novoselov, A. Mishchenko, A. Carvalho, and A. H. Castro Neto. 2d materials and van der waals heterostructures. *Science*, 353(6298):aac9439, jul 2016.

21 S. J. Haigh, A. Gholinia, R. Jalil, S. Romani, L. Britnell, D. C. Elias, K. S. Novoselov, L. A. Ponomarenko, A. K. Geim, and R. Gorbachev. Cross-sectional imaging of individual layers and buried interfaces of graphene-based heterostructures and superlattices. *Nature Materials*, 11(9):764–767, jul 2012.

22 Wei-Ting Hsu, Zi-Ang Zhao, Lain-Jong Li, Chang-Hsiao Chen, Ming-Hui Chiu, Pi-Shan Chang, Yi-Chia Chou, and Wen-Hao Chang. Second harmonic generation from artificially stacked transition metal dichalcogenide twisted bilayers. *ACS Nano*, 8(3):2951–2958, feb 2014.

23 Wenjing Zhang, Qixing Wang, Yu Chen, Zhuo Wang, and Andrew T S Wee. Van der waals stacked 2d layered materials for optoelectronics. *2D Materials*, 3(2):022001, apr 2016.

24 Humberto Terrones, Florentino López-Urías, and Mauricio Terrones. Novel hetero-layered materials with tunable direct band gaps by sandwiching different metal disulfides and diselenides. *Scientific Reports*, 3(1), mar 2013.

25 Anshul Kogar, Melinda S. Rak, Sean Vig, Ali A. Husain, Felix Flicker, Young Il Joe, Luc Venema, Greg J. MacDougall, Tai C. Chiang, Eduardo Fradkin, Jasper van Wezel, and Peter Abbamonte. Signatures of exciton condensation in a transition metal dichalcogenide. *Science*, 358(6368):1314–1317, dec 2017.

26 Pasqual Rivera, John R. Schaibley, Aaron M. Jones, Jason S. Ross, Sanfeng Wu, Grant Aivazian, Philip Klement, Kyle Seyler, Genevieve Clark, Nirmal J. Ghimire, Jiaqiang Yan, D. G. Mandrus, Wang Yao, and Xiaodong Xu. Observation of long-lived interlayer excitons in monolayer MoSe2–WSe2 heterostructures. *Nature Communications*, 6:6242, feb 2015.

27 Ming-Hui Chiu, Chendong Zhang, Hung-Wei Shiu, Chih-Piao Chuu, Chang-Hsiao Chen, Chih-Yuan S. Chang, Chia-Hao Chen, Mei-Yin Chou, Chih-Kang Shih, and Lain-Jong Li. Determination of band alignment in the single-layer MoS2/WSe2 heterojunction. *Nature Communications*, 6:7666, jul 2015.

28 H. Fang, C. Battaglia, C. Carraro, S. Nemsak, B. Ozdol, J. S. Kang, H. A. Bechtel, S. B. Desai, F. Kronast, A. A. Unal, G. Conti, C. Conlon, G. K. Palsson, M. C. Martin, A. M. Minor, C. S. Fadley, E. Yablonovitch, R. Maboudian, and A. Javey. Strong interlayer coupling in van der waals heterostructures built from single-layer chalcogenides. *Proceedings of the National Academy of Sciences*, 111(17):6198–6202, apr 2014.

29 Xiaoping Hong, Jonghwan Kim, Su-Fei Shi, Yu Zhang, Chenhao Jin, Yinghui Sun, Sefaattin Tongay, Junqiao Wu, Yanfeng Zhang, and Feng Wang. Ultrafast charge transfer in atomically thin MoS2/WS2 heterostructures. *Nature Nanotechnology*, 9(9):682–686, aug 2014.

30 Hoseok Heo, Ji Ho Sung, Soonyoung Cha, Bo-Gyu Jang, Joo-Youn Kim, Gangtae Jin, Donghun Lee, Ji-Hoon Ahn, Myoung-Jae Lee, Ji Hoon Shim, Hyunyong Choi, and Moon-Ho Jo. Interlayer orientation-dependent light absorption and emission in monolayer semiconductor stacks. *Nature Communications*, 6(1), jun 2015.

31 Yashwanth Balaji, Quentin Smets, Cesar Javier Lockhart De La Rosa, Anh Khoa Augustin Lu, Daniele Chiappe, Tarun Agarwal, Dennis H. C. Lin, Cedric Huyghebaert, Iuliana Radu, Dan Mocuta, and Guido Groeseneken. Tunneling transistors based on MoS2/MoTe2 van der waals heterostructures. *IEEE Journal of the Electron Devices Society*, 6:1048–1055, 2018.

32 Yan Chen, Xudong Wang, Guangjian Wu, Zhen Wang, Hehai Fang, Tie Lin, Shuo Sun, Hong Shen, Weida Hu, Jianlu Wang, Jinglan Sun, Xiangjian Meng, and Junhao Chu. High-performance photovoltaic detector based on MoTe2 /MoS2 van der waals heterostructure. *Small*, 14(9):1703293, jan 2018.

33 Ning Lu, Hongyan Guo, Lei Li, Jun Dai, Lu Wang, Wai-Ning Mei, Xiaojun Wu, and Xiao Cheng Zeng. MoS2/MX2 heterobilayers: bandgap engineering via tensile strain or external electrical field. *Nanoscale*, 6(5):2879–2886, 2014.

34 Jun Kang, Sefaattin Tongay, Jian Zhou, Jingbo Li, and Junqiao Wu. Band offsets and heterostructures of two-dimensional semiconductors. *Applied Physics Letters*, 102(1):012111, jan 2013.

35 G. Kresse and J. Furthmüller. Efficient iterative schemes for *ab initio* total-energy calculations using a plane-wave basis set. *Phys. Rev. B*, 54:11169–11186, 1996.

36 John P. Perdew, Kieron Burke, and Matthias Ernzerhof. Generalized gradient approximation made simple. *Phys. Rev. Lett.*, 77:3865–3868, 1996.

37 Stefan Grimme. Semiempirical gga-type density functional constructed with a long-range dispersion correction. *Journal of Computational Chemistry*, 27(15):1787–1799, 2006.

38 Stefan Grimme, Jens Antony, Stephan Ehrlich, and Helge Krieg. A consistent and accurate ab initio parametrization of density functional dispersion correction (DFT-d) for the 94 elements h-pu. *The Journal of Chemical Physics*, 132(15):154104, apr 2010.

39 Stefan Grimme, Stephan Ehrlich, and Lars Goerigk. Effect of the damping function in dispersion corrected density functional theory. *Journal of Computational Chemistry*, 32(7):1456–1465, mar 2011.

40 Jochen Heyd, Gustavo E. Scuseria, and Matthias Ernzerhof. Hybrid functionals based on a screened coulomb potential. *J. Chem. Phys.*, 118(18):8207–8215, 2003.

41 J. Heyd, G. E. Scuseria, and M. Ernzerhof. Erratum: éĹěæÿĽybrid functionals based on a screened coulomb potentialéĹě?[j. chem. phys. 118, 8207 (2003)]. *J. Chem. Phys.*, 124:219906, 2006.

42 Ling Tang, MengQiu Long, Dong Wang, and ZhiGang Shuai. The role of acoustic phonon scattering in charge transport in organic semiconductors: a first-principles deformation-potential study. *Sci. China Ser. B*, 52(10):1646–1652, 2009.

43 Y. Cai, G. Zhang, and Y.W Zhang. Polarity-reversed robust carrier mobility in monolayer mos_2 nanoribbons. *J. Am. Chem. Soc.*, 136:6269–6275, 2014.

44 Mengqiu Long, Ling Tang, Dong Wang, Yuliang Li, and Zhigang Shuai. Electronic structure and carrier mobility in graphdiyne sheet and nanoribbons: Theoretical predictions. *ACS Nano.*, 5(4):2593–2600, 2011.

45 J. Chen, J. Xi, D. Wang, and Z Shuai. Carrier mobility in graphyne should be even larger than that in graphene: A theoretical prediction. *J. Phys. Chem. Lett.*, 4:1443–1448, 2013.

46 Yanli Wang and Yi Ding. Electronic structure and carrier mobilities of arsenene and antimonene nanoribbons:a first-principle study. *Nanoscale Res. Lett.*, 10:254, 2015.

47 J. Bardeen and W. Shockley. Deformation potentials and mobilities in non-polar crystals. *Phys. Rev.*, 80:72–80, 1950.

48 W. Walukiewicz, H. E. Ruda, J. Lagowski, and H. C. Gatos. Electron mobility in modulation-doped heterostructures. *Physical Review B*, 30(8):4571–4582, oct 1984.

49 Shin ichi Takagi, Judy L. Hoyt, Jeffrey J. Welser, and James F. Gibbons. Comparative study of phonon-limited mobility of two-dimensional electrons in strained and unstrained si metal–oxide–semiconductor field-effect transistors. *Journal of Applied Physics*, 80(3):1567–1577, aug 1996.

50 J.A. Wilson and A.D. Yoffe. The transition metal dichalcogenides discussion and interpretation of the observed optical, electrical and structural properties. *Advances in Physics*, 18(73):193–335, may 1969.

51 Ganesh R. Bhimanapati, Zhong Lin, Vincent Meunier, Yeonwoong Jung, Judy Cha, Saptarshi Das, Di Xiao, Youngwoo Son, Michael S. Strano, Valentino R. Cooper, Liangbo Liang, Steven G. Louie, Emilie Ringe, Wu Zhou, Steve S. Kim, Rajesh R. Naik, Bobby G. Sumpter, Humberto Terrones, Fengnian Xia, Yeliang Wang, Jun Zhu, Deji Akinwande, Nasim Alem, Jon A. Schuller, Raymond E. Schaak, Mauricio Terrones, and Joshua A. Robinson. Recent Advances in Two-Dimensional Materials beyond Graphene. *ACS Nano*, 9(12):11509–11539, 2015.

52 Huabing Shu, Yunhai Li, Xianghong Niu, and Jinlan Wang. The stacking dependent electronic structure and optical properties of bilayer black phosphorus. *Physical Chemistry Chemical Physics*, 18(8):6085–6091, 2016.

53 Kaihui Liu, Liming Zhang, Ting Cao, Chenhao Jin, Diana Qiu, Qin Zhou, Alex Zettl, Peidong Yang, Steve G. Louie, and Feng Wang. Evolution of interlayer coupling in twisted molybdenum disulfide bilayers. *Nature Communications*, 5(1), sep 2014.

54 Birman J L Burns G. *Introduction to Group Theory with Applications*. Academic Press, 1977.

55 J. H. Rose, John Ferrante, and John R. Smith. Universal binding energy curves for metals and bimetallic interfaces. *Physical Review Letters*, 47(9):675–678, aug 1981.

56 Jun Zhao, Yanle Li, and Jing Ma. Quantum spin hall insulators in functionalized arsenene (asx, x = f, oh and ch3) monolayers with pronounced light absorption. *Nanoscale*, 8:9657–9666, 2016.

57 Shiyuan Gao, Li Yang, and Catalin D. Spataru. Interlayer coupling and gate-tunable excitons in transition metal dichalcogenide heterostructures. *Nano Letters*, 17(12):7809–7813, nov 2017.

58 Ziheng Ji, Hao Hong, Jin Zhang, Qi Zhang, Wei Huang, Ting Cao, Ruixi Qiao, Can Liu, Jing Liang, Chuanhong Jin, Liying Jiao, Kebin Shi, Sheng Meng, and Kaihui Liu. Robust stacking-independent ultrafast charge transfer in MoS2/WS2 bilayers. *ACS Nano*, nov 2017.

59 B. Amin, N. Singh, and U. SchwingenschlæđŽgl. Heterostructures of transition metal dichalcogenides. *Physical Review B*, 92(7), aug 2015.

60 Zhida Zheng, Xiaocha Wang, and Wenbo Mi. Strain and electric-field tunable valley states in 2d van der waals MoTe2/WTe2heterostructures. *Journal of Physics: Condensed Matter*, 28(50):505003, oct 2016.

61 Bin Amin, Thaneshwor P. Kaloni, Georg Schreckenbach, and Michael S. Freund. Materials properties of out-of-plane heterostructures of MoS2-WSe2 and WS2-MoSe2. *Applied Physics Letters*, 108(6):063105, feb 2016.

62 Ning Lu, Hongyan Guo, Lei Li, Jun Dai, Lu Wang, Wai-Ning Mei, Xiaojun Wu, and Xiao Cheng Zeng. MoS2/MX2 heterobilayers: bandgap engineering via tensile strain or external electrical field. *Nanoscale*, 6(5):2879–2886, 2014.

63 Hong Jiang. Electronic band structures of molybdenum and tungsten dichalcogenides by the GW approach. *The Journal of Physical Chemistry C*, 116(14):7664–7671, mar 2012.

64 Yi Ding, Yanli Wang, Jun Ni, Lin Shi, Siqi Shi, and Weihua Tang. First principles study of structural, vibrational and electronic properties of graphene-like MX2 (m=mo, nb, w, ta;x=s, se, te) monolayers. *Physica B: Condensed Matter*,

406(11):2254–2260, may 2011.

65 K. Kośmider and J. Fernández-Rossier. Electronic properties of the MoS2-WS2heterojunction. *Physical Review B*, 87(7), feb 2013.

66 Wolfgang G. Zeier, Alex Zevalkink, Zachary M. Gibbs, Geoffroy Hautier, Mercouri G. Kanatzidis, and G. Jeffrey Snyder. Thinking like a chemist: Intuition in thermoelectric materials. *Angew. Chem. Int. Ed.*, 55(24):6826–6841, 2016.

67 R. L. Anderson. Germanium-gallium arsenide heterojunctions [letter to the editor]. *IBM Journal of Research and Development*, 4(3):283–287, jul 1960.

68 N Vol. What is what in the nanoworld: A handbook on nanoscience and nanotechnology. *Materials Today*, 7(12):49, dec 2004.

69 H. Fang, C. Battaglia, C. Carraro, S. Nemsak, B. Ozdol, J. S. Kang, H. A. Bechtel, S. B. Desai, F. Kronast, A. A. Unal, G. Conti, C. Conlon, G. K. Palsson, M. C. Martin, A. M. Minor, C. S. Fadley, E. Yablonovitch, R. Maboudian, and A. Javey. Strong interlayer coupling in van der waals heterostructures built from single-layer chalcogenides. *Proceedings of the National Academy of Sciences*, 111(17):6198–6202, apr 2014.

70 Shengli Zhang, Meiqiu Xie, Fengyu Li, Zhong Yan, Yafei Li, Erjun Kan, Wei Liu, Zhongfang Chen, and Haibo Zeng. Semiconducting group 15 monolayers: A broad range of band gaps and high carrier mobilities. *Angew. Chem. Int. Ed.*, 55(5):1666–1669, 2016.

71 Ming-Hui Chiu, Chendong Zhang, Hung-Wei Shiu, Chih-Piao Chuu, Chang-Hsiao Chen, Chih-Yuan S. Chang, Chia-Hao Chen, Mei-Yin Chou, Chih-Kang Shih, and Lain-Jong Li. Determination of band alignment in the single-layer MoS2/WSe2 heterojunction. *Nature Communications*, 6:7666, jul 2015.

72 Bo Peng, Hao Zhang, Hezhu Shao, Ke Xu, Gang Ni, Jing Li, Heyuan Zhu, and Costas M. Soukoulis. Chemical intuition for high thermoelectric performance in monolayer black phosphorus, alpha-arsenene and aw-antimonene. *Journal of Materials Chemistry A*, 6(5):2018–2033, 2018.

73 Sverre Froyen and Walter A. Harrison. Elementary prediction of linear combination of atomic orbitals matrix elements. *Phys. Rev. B*, 20:2420–2422, Sep 1979.

74 Aubrey T. Hanbicki, Hsun-Jen Chuang, Matthew R. Rosenberger, C. Stephen Hellberg, Saujan V. Sivaram, Kathleen M. McCreary, Igor I. Mazin, and Berend T. Jonker. Double indirect interlayer exciton in a MoSe2/WSe2 van der waals heterostructure. *ACS Nano*, 12(5):4719–4726, may 2018.

75 Jun Kang, Jingbo Li, Shu-Shen Li, Jian-Bai Xia, and Lin-Wang Wang. Electronic structural moiré pattern effects on MoS2/MoSe2 2d heterostructures. *Nano Letters*, 13(11):5485–5490, oct 2013.

76 Félix Mouhat and François-Xavier Coudert. Necessary and sufficient elastic stability conditions in various crystal systems. *Physical Review B*, 90(22), dec 2014.

77 Bo Peng, Hao Zhang, Hezhu Shao, Zeyu Ning, Yuanfeng Xu, Gang Ni, Hongliang Lu, David Wei Zhang, and Heyuan Zhu. Stability and strength of atomically thin borophene from first principles calculations. *Materials Research Letters*, 5(6):399–407, November 2017.

78 R. C. Andrew, R. E. Mapasha, A. M. Ukpong, and N. Chetty. Mechanical properties of graphene and boronitrene. *Physical Review B*, 85(12), mar 2012.

79 Fan Zeng, Wei-Bing Zhang, and Bi-Yu Tang. Electronic structures and elastic properties of monolayer and bilayer transition metal dichalcogenides MX2 (m = mo, w; x = o, s, se, te): A comparative first-principles study. *Chinese Physics B*, 24(9):097103, sep 2015.

80 Liping Yu, Qimin Yan, and Adrienn Ruzsinszky. Negative poisson's ratio in 1t-type crystalline two-dimensional transition metal dichalcogenides. *Nature Communications*, 8:15224, may 2017.

81 M. Gajdoš, K. Hummer, G. Kresse, J. Furthmüller, and F. Bechstedt. Linear optical properties in the projector-augmented wave methodology. *Phys. Rev. B*, 73:045112, 2006.

82 Yuanfeng Xu, Bo Peng, Hao Zhang, Hezhu Shao, Rongjun Zhang, and Heyuan Zhu. First-principle calculations of optical properties of monolayer arsenene and antimonene allotropes. *Ann. Phys. (Berlin)*, page 1600152, 2017.

83 MS Dresselhaus. *Solid State Physics Part II Optical Properties of Solids*. Citeseer, 1999.

84 Sonali Saha, T. P. Sinha, and Abhijit Mookerjee. Electronic structure, chemical bonding, and optical properties of paraelectric $batio_3$. *Phys. Rev. B*, 62:8828–8834, 2000.

85 Bingcheng Luo, Xiaohui Wang, Enke Tian, Guowu Li, and Longtu Li. Electronic structure, optical and dielectric properties of $batio_3/catio_3/srtio_3$ ferroelectric superlattices from first-principles calculations. *J. Mater. Chem. C*, 3:8625–8633, 2015.

86 Ji-Hui Yang, Yueyu Zhang, Wan-Jian Yin, XG Gong, Boris I Yakobson, and Su-Huai Wei. Two-dimensional sis layers with promising electronic and optoelectronic properties: theoretical prediction. *Nano letters*, 16(2):1110–1117, 2016.

87 Yuanfeng Xu, Hao Zhang, Hezhu Shao, Gang Ni, Jing Li, Hongliang Lu, Rongjun Zhang, Bo Peng, Yongyuan Zhu, Heyuan Zhu, and Costas M. Soukoulis. First-principles study on the electronic, optical, and transport properties of monolayer alpha - and beta -GeSe. *Physical Review B*, 96(24), dec 2017.